Accelerating GW calculations of point defects with the defect-patched screening approximation

Du L‡, Zhen-Fei Liu*,§, and Li Yang†,‡, |

[‡]Department of Physics, Washington University in St. Louis, St. Louis, Missouri 63130, USA

§Department of Chemistry, Wayne State University, Detroit, Michigan 48202, USA

Institute of Materials Science and Engineering, Washington University in St. Louis, St. Louis, Missouri 63130, USA

ABSTRACT: The *GW* approximation has been widely accepted as an *ab initio* tool for calculating defect levels with many-electron effect included. However, the *GW* simulation cost increases dramatically with the system size, and, unfortunately, large supercells are often required to model low-density defects that are experimentally relevant. In this work, we propose to accelerate *GW* calculations of point defects by reducing the simulation cost of the many-electron screening, which is the primary computational bottleneck. The random-phase approximation of many-electron screening is divided into two parts: one is the intrinsic screening, calculated using a unit cell of pristine structures, and the other is the defect-induced screening, calculated using the supercell within a small energy window. Depending on specific defects, one may only need to consider the intrinsic screening or include the defect

contribution. This approach avoids the summation of many conductions states of supercells and significantly reduces the simulation time. We have applied it to calculating various point defects, including neutral and charged defects in two-dimensional and bulk systems with small or large bandgaps. The results consist with those from the direct GW simulations. This defect-patched screening approach not only clarifies the roles of defects in many-electron screening but also paves the way to fast screen defect structures/materials for novel applications, including single-photon sources, quantum qubits, and quantum sensors.

1. Introduction

Point defects decide a wide range of fundamental materials properties, such as transport, optical, and magnetic properties. For example, certain defects are responsible for features in optical spectra and hence the name of "color centers", such as ultraviolet color centers in zinc oxide and cubic boron nitride¹⁻⁵, visible and near-infrared color centers in diamond and silicon carbide.⁶⁻¹⁹ In recent years, there has been growing interest in applying materials with point defects in single-photon sources, quantum qubits, and quantum sensors.^{20,21} For instance, in diamond and silicon carbide, point defects not only act as quantum emitters and sensors but also possess spins that can be used to implement isolated quantum qubits.^{14-18,22,23} Point defects in two-dimensional (2D) materials, such as chalcogen vacancies in 2D transition-metal dichalcogenides (TMDs) and point defects in layered hexagonal boron nitride (*h*-BN), have attracted significant attention for single-photon emitters²⁴⁻³³ and quantum qubits³⁴⁻³⁷. These

defects in 2D materials can have close interactions with the environments, making them promise for quantum sensing^{38,39}.

Ab initio electronic structure methods are indispensable in predicting microscopic structureproperty relationships for defect systems. It is by now common knowledge that the local and semi-local exchange-correlation functionals within the framework of Kohn-Sham (KS) density functional theory (DFT) tend to underestimate the band gap of materials and may not provide accurate descriptions of the defect energy levels and how these levels are aligned with the band edges of the otherwise pristine material. 40,41 To overcome this limitation, the GW approximation within the framework of many-body perturbation theory (MBPT)^{42,43} is a popular choice and has been shown to be quantitatively accurate for a broad range of defects. 41,44-47 However, when it is implemented using a plane-wave basis that is suitable for periodic systems, a large number of empty states need to be included in the calculation to converge the non-interacting KS polarizability, which is the computational bottleneck for calculating point defects in large supercells. To date, many methods have been proposed to make the calculations of large systems more tractable. The large number of empty states can be approximated by free-electron states⁴⁸ or be eliminated using the Sternheimer equation.⁴⁹ Moreover, calculations can be simplified by replacing the widely used plane-wave basis with others, such as Wannier orbitals⁵⁰⁻⁵², projected-dielectric eigen-decomposition basis⁵³⁻⁵⁶, or stochastic orbitals^{57,58}, etc. However, these approaches require additional techniques to

transform between different basis. In this work, we propose an accelerated GW approach in plane-wave basis, which is generally applicable to a broad range of defect systems.

We focus on overcoming the major computational bottleneck, namely the noninteracting KS polarizability within the random-phase approximation (RPA), in GW calculations of point defects. We present two-level approximations: intrinsic screening approximation and defectpatched screening approximation. At the first level, we approximate the RPA polarizability of a defect-containing supercell by that of the pristine structure, realized by the reciprocal-space folding.⁵⁹ This reduces the polarizability calculation to a unit cell, and the calculated defect levels excellently agree with the direct GW ones when the minimum energy gap between defect levels is close to the bulk band gap of the parent materials. Otherwise, if the defect gaps are substantially smaller than the bulk bandgap, we further include the defect-contributed RPA polarizability but only compute this contribution within a small energy window. As a result, this defect-patched approximation avoids including many unoccupied states to obtain the RPA polarizability, significantly reducing the computational cost. We demonstrate the strength of this approach in obtaining defect levels of a wide range of defect structures, including neutral and charged defects in 2D or bulk insulators and semiconductors. The agreements between the defect-patched approximation and direct GW result are excellent. Such an accelerated GW approach can serve as a powerful tool to screen point defects with desired defect levels for broad applications.

The structure of this article is as follows. In Section 2, we discuss the theoretical framework to calculate quasiparticle energies of point defect systems, showing the main assumptions to simplify the calculation of RPA polarizability. In Section 3, we demonstrate the strengths of our approach using various examples: the double carbon substitutional defect in *h*-BN in Section 3 A; the single selenium vacancy in monolayer MoSe₂ in Section 3 B; the single boron vacancy in monolayer *h*-BN in Section 3 C; the negatively charged NV center in diamond in Section 3 D. In Section 4, we provide the comparison of computational efficiency. We conclude our work in Section 5.

2. Theoretical Approach

In the GW approximation, quasiparticle self-energy is calculated via $\Sigma = iGW$, ^{42,43} where G is the Green's function and W is the screened Coulomb interaction. The primary bottleneck of ab initio GW calculations is the high computational cost and memory requirement of the noninteracting RPA polarizability, χ^0 . In reciprocal space, the χ^0 of insulators is:

$$\chi_{GG'}^{0}(\boldsymbol{q},\omega) = \sum_{v,c,k} \frac{\left\langle v, \boldsymbol{k} + \boldsymbol{q} \middle| e^{i(\boldsymbol{q}+\boldsymbol{G})\cdot\boldsymbol{r}} \middle| c, \boldsymbol{k} \right\rangle \left\langle c, \boldsymbol{k} \middle| e^{-i(\boldsymbol{q}+\boldsymbol{G}')\cdot\boldsymbol{r}'} \middle| v, \boldsymbol{k} + \boldsymbol{q} \right\rangle}{\omega + E_{v,k+q} - E_{c,k}}, \tag{1}$$

where q and k are vectors in the first Brillouin zone, G is a reciprocal-space lattice vector. v refers to occupied valence states and c refers to unoccupied conduction states. $|v, k + q\rangle$, $|c, k\rangle$, $E_{v,k+q}$, and $E_{c,k}$ are the KS eigenvectors and eigenvalues, respectively. In plane-wave basis, Eq. (1) leads to a formal scaling of $O(N^4)$ or a practical scaling of $O(N^3)$ of $O(N^4)$, where N corresponds

to the system size. To model isolated point defects or dilute defects of experimental relevance, a large supercell is needed, resulting in high computational cost.

To make the GW calculations more tractable, we approximate the RPA polarizability χ^0 of a supercell with a point defect as:

$$\chi^0 \approx \chi^0_{\text{Intrinsic}} + \chi^0_{\text{Defect}}.$$
 (2)

 $\chi^0_{\mathrm{Intrinsic}}$ is the polarizability of the supercell without defect, which is essentially the intrinsic screening of the parent material. χ^0_{Defect} is the contribution from the point defect. In the following, we simplify the calculation of $\chi^0_{\mathrm{Intrinsic}}$ and χ^0_{Defect} , respectively.

 $\chi^0_{\mathrm{Intrinsic}}$ of the supercell is essentially the polarizability of pristine structures, which can be obtained by computing the χ^0 from a pristine primitive cell followed by the reciprocal-space folding procedure⁵⁹. This idea was originally developed in the context of weakly coupled molecule-substrate interfaces.^{59,61} In this approach, the RPA polarizability of a supercell can be written as $\chi^0_{\mathrm{Intrinsic}}(q+G,q+G')$, where G,G' are reciprocal lattice vectors and G is a vector in the first Brillouin zone of the supercell. Similarly, the RPA polarizability of the primitive cell can be written as $\tilde{\chi}^0_{\mathrm{Intrinsic}}(\tilde{q}+\tilde{G},\tilde{q}+\tilde{G}')$, where \tilde{G},\tilde{G}' are the reciprocal lattice vectors and \tilde{G} is a vector in the first Brillouin zone of the primitive cell. $\chi^0_{\mathrm{Intrinsic}}$ and $\tilde{\chi}^0_{\mathrm{Intrinsic}}$ describe the same quantity, i.e., $\chi^0_{\mathrm{Intrinsic}}(q+G,q+G')=\tilde{\chi}^0_{\mathrm{Intrinsic}}(\tilde{G}+\tilde{G},\tilde{G}+\tilde{G}')$, where G is an G is an G in the first Brillouin zone of the primitive cell.

Therefore, the supercell form, $\chi^0_{\mathrm{Intrinsic}}(\boldsymbol{G},\boldsymbol{G}';\boldsymbol{q})$, can be obtained from the primitive-cell form, $\widetilde{\chi}^0_{\mathrm{Intrinsic}}(\widetilde{\boldsymbol{G}},\widetilde{\boldsymbol{G}}';\widetilde{\boldsymbol{q}})$.

It is challenging to directly calculate the second term ($\chi^0_{\rm Defect}$) in Eq. (2). Fortunately, in diluted defect densities, the density of defect states is much smaller than that of the background crystal. This is also the typical experimental situation. Thus, $\chi^0_{\rm Defect}$ can be regarded as a small correction. More quantitatively, according to the denominator of Eq. (1), the main contribution to polarizability is from the transitions between defect levels with small energy differences. Therefore, it is possible to calculate the defect contribution within an energy window. This idea was originally developed in the context of strongly coupled molecule-metal interfaces.⁶² We propose to calculate the defect-contributed polarizability as:

$$\chi_{\text{Defect}}^{0}(\boldsymbol{q},\omega) = \sum_{\substack{v,c,k\\E_{v,k+q},E_{c,k}\in[E_{\min},E_{\max}]}} \frac{\langle v,\boldsymbol{k}+\boldsymbol{q}|e^{i(\boldsymbol{q}+\boldsymbol{G})\cdot\boldsymbol{r}}|c,\boldsymbol{k}\rangle\langle c,\boldsymbol{k}|e^{-i(\boldsymbol{q}+\boldsymbol{G}')\cdot\boldsymbol{r}'}|v,\boldsymbol{k}+\boldsymbol{q}\rangle}{\omega+E_{v,k+q}-E_{c,k}}$$

$$-\sum_{\substack{v,c,k\\v,c\in\text{Intrinsic}\\E_{v,k+q},E_{c,k}\in[E_{\min},E_{\max}]}} \frac{\langle v,\boldsymbol{k}+\boldsymbol{q}|e^{i(\boldsymbol{q}+\boldsymbol{G})\cdot\boldsymbol{r}}|c,\boldsymbol{k}\rangle\langle c,\boldsymbol{k}|e^{-i(\boldsymbol{q}+\boldsymbol{G}')\cdot\boldsymbol{r}'}|v,\boldsymbol{k}+\boldsymbol{q}\rangle}{\omega+E_{v,k+q}-E_{c,k}},$$

(3)

where the first term contains all transitions within the defined energy window $[E_{\min}, E_{\max}]$, including defect-defect, defect-bulk, and bulk-bulk contributions. The second term removes the non-defect contributions and removes the double counting. Although the defect polarization is calculated in supercells, it quickly converges as the energy window is

increased. In all our calculated defect structures, the converged energy window only needs to extend into band edges around 1 eV. This defect-patched approximation avoids the bottleneck of the direct RPA polarizability calculation in Eq. (1), which requires a significant number of unoccupied bands/states of supercells.

In the following, we show that, depending on specific defects, one may only need to consider the intrinsic polarizability or include the defect contribution. These two tiers of approaches accelerate the GW calculations of defects and make it possible to accurately screen a large number of defect systems for targeted applications.

3. Applications

In this section, we demonstrate the accuracy of our approximations by comparing them with the direct GW calculations for several typical point defects of broad interests. Unless otherwise specified, the computational details of this section are as follows. The DFT calculation is performed using the Perdew-Burke-Ernzerhof (PBE) exchange-correlation functional⁶³ and a plane-wave energy cutoff of 60 Ry with the QUANTUM ESPRESSO package⁶⁴. For two-dimensional (2D) structures, the vdW interaction is included via the semi-empirical Grimme-D3 scheme⁶⁵. A vacuum of 18 Å between adjacent layers is used to avoid spurious interactions between periodic images along the out-of-plane direction for 2D structures. The GW calculations are performed using the BERKELEYGW package with our modifications of the calculating of polarizability⁶⁰ presented in Section 2. All GW calculations reported in this work

are perturbative, i.e., G_0W_0 . The Hybertsen-Louie generalized plasmon-pole model is used to treat the frequency dependence of the dielectric function⁴². The static remainder approximation⁶⁶ is used in the evaluation of the self-energy for faster convergence. The slab Coulomb truncation⁶⁷ is adopted to mimic suspended 2D structures.

A. Double carbon substitutional defects in monolayer *h*-BN

The first example is the double carbon substitutional defect (C_BC_N) in monolayer hexagonal boron nitride (h-BN), and it is proposed to be a candidate of single-photon emitters. As shown in Fig. 1(a), this defect is formed by replacing two neighboring boron and nitrogen atoms with a pair of carbon atoms. We construct a $9 \times 9 \times 1$ supercell with a point defect, corresponding to a 1.2% defect concentration. A $2 \times 2 \times 1$ q-grid is adopted to calculate the polarizability and quasiparticle energies in the supercell. Around 8,000 empty states are included in the direct GW calculation of the RPA polarizability.

Fig. 1(b) presents the DFT electronic structure, where the gray lines are continuous bulk bands of *h*-BN, and the two blue lines are the defect energy levels lying inside the gap. To better illustrate how the defect levels are aligned in energy with the band edges of the *h*-BN, a schematic energy diagram is plotted in Fig. 1(c). As shown in Fig. (c), the minimum energy difference between occupied and unoccupied defect states is 3.58 eV, which is defined as the "defect gap" in this article. Meanwhile, the energy gap between continuum bulk states of *h*-BN is 4.68 eV, which we define as the "bulk bandgap" and is essentially the bandgap of pristine

structures. The distance between the lower-energy defect level and the valance band maximum (VBM) of bulk states is 45 meV, and that between the higher-energy defect level and the conduction band minimum (CBM) is 65 meV. These results agree with previous DFT calculations.⁷⁰

Fig. 1(d) shows the quasiparticle defect levels of this $9 \times 9 \times 1$ supercell with a C_BC_N defect from a direct *GW* calculation. As expected, the reduced screening of such a 2D structure significantly enhances the self-energy correction. The bulk bandgap is increased from 4.68 eV to 7.29 eV, and the defect gap is increased from 3.58 eV to 6.38 eV.

We first neglect defect contribution and only consider the intrinsic screening in the GW calculation ($\chi^0 \approx \chi^0_{\rm Intrinsic}$, i.e., only including the first term in Eq. (2)). This will be called "intrinsic screening approximation" in this paper. The results are presented in Fig. 1(e). The quasiparticle bulk bandgap of h-BN is 7.32 eV, and the defect gap is 6.43 eV. Compared to the direct GW results, the agreements are surprisingly good, and the difference is within 50 meV.

Then we further consider the "defect-patched screening approximation" by adding the defect contribution to the polarizability, i.e., including both terms in Eq. (2) with the second term computed via Eq. (3). We find that the result converges within a relatively narrow energy window. For this defect, the energy window of summation is set to be 1.8 eV below the VBM and 1.7 eV above the CBM of bulk h-BN, as marked by the black-dash lines in Fig. 1 (b). The GW results are plotted in Fig. 1(f), in which the bulk bandgap of h-BN is 7.31 eV and the defect

gap is 6.41 eV. The difference in the defect gap between the direct GW and defect-patched screening approximation is slightly improved to be within 30 meV, compared with the intrinsic screening approximation (Fig. 1(e)).

The success of intrinsic screening approximation and the small defect contribution to the polarizability are expected, and the reason can be seen from Eq. (3). The polarizability is affected by transition energy, which is strongly affected by defect gap. For the CBCN defect, the defect gap is large (comparable to the bulk bandgap), resulting in a large dominator in Eq. (3). As a result, the defect contribution is negligible, making the intrinsic screening approximation reliable.

This explanation can be further justified by comparing the RPA polarizability matrices in plane-wave basis. The matrix elements of the polarizability of the direct GW calculation are plotted in Fig. 2(a), and the difference from the intrinsic polarizability ($\chi^0 - \chi^0_{\rm Intrinsic}$) is plotted in Fig. 2(b). We can easily find that the difference is about two orders of magnitude smaller than that of the directly-calculated χ^0 , numerically justifying the intrinsic screening approximation. We have further plotted the matrix elements of $\chi^0_{\rm Defect}$ in Fig. 2(b). Their magnitude is also about two orders of smaller than those of the directly-calculated χ^0 , supporting that the defect contribution to the polarizability is negligible.

Finally, considering the experimentally relevant diluted defect densities, where the density of defect states will be much lower than that in the $9 \times 9 \times 1$ supercell. As a result, the defect

contribution to the total polarizability will be even smaller for diluted defect densities, further supporting the intrinsic screening approximation. Therefore, we expect that the intrinsic screening approximation is reliable for defect structures with a large defect gap.

B. Single selenium vacancy in monolayer MoSe₂

In this section, we investigate a selenium vacancy (V_{Se}) in monolayer MoSe₂, which is formed by removing a single selenium atom in monolayer MoSe₂ as illustrated in Fig. 3(a). V_{Se} in monolayer MoSe₂ and many other similar point defects in layered TMD are important structures that can be used to realize 2D single-photon emitters.²⁴⁻²⁸ In our simulation, a $5 \times 5 \times 1$ MoSe₂ supercell is constructed corresponding to a 2% vacancy concentration. A q-grid of $3 \times 3 \times 1$ is adopted to calculate the dielectric function and quasiparticle energies in the supercell. Around 4,300 empty states are included in the direct calculation of the RPA polarizability.

The DFT band structure and corresponding schematic energy diagram are shown in Fig. 3(b) and Fig. 3(c), respectively. The DFT bulk bandgap of monolayer MoSe₂ is 1.43 eV. There are nearly double-degenerate unoccupied defect states inside the bandgap, which are labeled by a dashed line in Fig. 3(c). In this case, the defect gap is 1.03 eV, corresponding to the energy gap between these unoccupied defect levels and the highest occupied state, i.e., the VBM of MoSe₂. The defect gap (1.03 eV) is comparable with the intrinsic bulk bandgap (1.43 eV) of monolayer MoSe₂, making it another ideal example of large defect-gap systems.

The direct GW results are presented in Fig. 3(d), in which the bulk bandgap is increased to 2.36 eV and the defect gap is increased to 1.78 eV. These results agree with previous GW calculations.⁷¹ The GW results within the intrinsic screening approximation are shown in Fig. 3(e). The bulk band gap is 2.39 eV, and the defect gap is 1.86 eV, respectively, which agree well with the direct GW results. The results using the defect-patched screening approximation are shown in Fig. 3(f). As expected, the calculated bulk band gap is 2.38 eV, and the defect gap is 1.82 eV, which are slightly closer to the direct GW result.

C. Single boron vacancy in monolayer h-BN

In this section, we study the charge-neutral single boron vacancy (V_B) in monolayer h-BN, where a single boron is removed to form a vacancy defect as Fig. 4(a) shows. A $9 \times 9 \times 1$ h-BN supercell is constructed corresponding to a 1.2% vacancy concentration. Following previous works⁷², DFT calculation is performed using the local spin density approximation (LSDA).⁷³ A q-grid of $2 \times 2 \times 1$ is adopted to calculate the dielectric function and quasiparticle energies in the supercell. Around 8,000 conduction states are included in the direct GW calculation.

The DFT band structure is shown Fig. 4(b), and the corresponding band alignment is plotted in Fig. 4(c). Our study shows that V_B in monolayer *h*-BN has a doublet ground state, which agrees with previous DFT study.⁷⁴ There are three in-gap defect states, and all of them are unoccupied. Different from the defects discussed in Section 3 A and B, these in-gap defect states are close to the VBM of *h*-BN. As marked in Fig. 4 (c), the spin-up defect gap is 151 meV,

and the spin-down defect gap is 320 meV. Thus, this is a good example of studying narrow defect-gap systems.

The result of the direct GW calculation is presented in Fig. 4(d), where the quasiparticle bulk bandgap of h-BN is increased to 7.05 eV. The spin-up defect gap is increased to 2.66 eV, and the spin-down defect gap is increased to 2.87 eV. Fig. 4 (e) shows the GW results within the intrinsic screening approximation. The bulk band gap is increased to 7.26 eV, the spin-up defect gap is 2.84 eV, and the spin-down defect gap is 3.13 eV. Compared to the direct GW results, the deviations are around 200-300 meV, which are significantly larger than those large defect-gap point defects discussed in Section 3 A and B.

This deviation is because the defect gap of the V_B defect in h-BN is significantly smaller than the bulk bandgap. According to Eq. (3), it leads to a small transition energy and hence a sizable contribution associated defect levels. Therefore, for narrow defect-gap systems, it is essential to include the defect contributions, leading us to the defect-patched screening approximation. The defect-patched screening results are presented in Fig. 4(f). We find a spin-up defect gap of 2.74 eV and a spin-down defect gap of 2.96 eV. The deviations from the direct GW calculation are reduced to 80 meV and 90 meV for the spin-up and spin-down defect gaps, respectively.

This improvement can also be quantitatively explained by comparing the magnitude of the matrix elements of RPA polarizability, as plotted in Fig. 5. Total polarizability by the direct

GW calculation is presented in Fig. 5(a), and the defect contribution is plotted in Fig. 5(b). Comparing to those of large defect-gap systems shown in Fig. 2(a) and (c), we can clearly see that the defect contribution in the narrow defect-gap system is much larger. The matrix elements of $\chi^0_{\rm Defect}$ is only about one order of magnitude smaller than those of directly calculated χ^0 in this charge-neutral single boron vacancy. Interestingly, we notice that the improvement of the defect-patched approximation is about 200-300 meV, which is also an order of magnitude of smaller than the GW self-energy corrections. Finally, Fig. 5(c) shows the validity of the defect-patched approximation, where the matrix elements of $\chi^0 - \chi^0_{\rm Intrinsic} - \chi^0_{\rm Defect}$ are near negligible. Therefore, for point defect systems with a defect gap significantly smaller than the bulk bandgap, it is necessary to use the defect-patched screening approximation.

D. Negatively charged NV center in diamond

Negatively charged NV centers in diamond are discussed in this section as an example of a charged point defect in a bulk material. The NV center consists of a substitutional nitrogen atom associated with a vacancy in the neighboring lattice site as shown in Fig. 6(a). NV centers are well-known candidates for realizing quantum qubit, and their spin can be initialized and read out through spin dependent decay processes by an optical approach (22,23). We use a $3 \times 3 \times 3$ supercell that contains 215 atoms to model this defect system, corresponding to a 0.46% vacancy concentration. A single Γ -point sampling is employed in the supercell calculations. Around 4,000 conduction states are included in the direct GW calculation.

The DFT band structure and corresponding band alignment are shown in Figs. 6(b) and 6(c), respectively. Our study shows that the negatively charged NV center in diamond has a triplet ground state, which agrees with previous DFT calculations⁷⁵ and first-principles MBPT and configuration interaction⁷⁶. The DFT-calculated bulk bandgap of diamond is 4.27 eV. As shown in Fig. 6(c), there are three occupied spin-up defect states inside the bulk bandgap, one singly occupied with lower energy and one pair of doubly occupied states with higher energy. There are three spin-down defect states, one occupied state and two doubly degenerate unoccupied states. The spin-conserved defect gap is 1.88 eV, measured as the energy difference between the lowest unoccupied spin-down defect state and the highest occupied spin-down defect state. The spin non-conserved defect gap is 1.27 eV, measured as the minimum energy difference between unoccupied and occupied defect states without considering spin. The quasiparticle energy levels calculated by the direct GW are shown in Fig. 6(d). The bulk bandgap increases to 5.14 eV. The spin-conserved gap increases to 2.81 eV, and the spin non-conserved gap increases to 2.14 eV. These results agree well with previous DFT and GW calculations.^{47,77}

We first show the results from the intrinsic screening approximation in Fig. 6(e). The quasiparticle bulk bandgap of diamond is $5.15 \, \text{eV}$, in good agreement with the direct GW result. The spin-conserved defect gap is $2.79 \, \text{eV}$, and the spin non-conserved defect gap is $2.36 \, \text{eV}$. Compared to the direct GW result in Fig. 6(d), there is a $220 \, \text{meV}$ deviation in the spin non-conserved gap, indicating that the screening effect from the charged NV center defect cannot be completely neglected. This also agrees with the aforementioned picture that, if the

defect gap is significantly smaller than the bulk bandgap, the defect contribution to the polarizability is non-negligible.

As expected, we find that the defect-patched screening approximation substantially improves the convergence. As shown in Fig. 6(f), the spin-conserved defect gap is corrected to 2.81 eV and spin non-conserved defect gap is corrected to 2.14 eV. The deviations from the direct *GW* results are reduced to within 10 meV. Such excellent agreements justify again the defect-patched screening approximation for small defect-gap systems.

Finally, we note that accurate calculations of quasiparticle energies and multiplet structures of open-shell defects need to go beyond the above single-shot G_0W_0 framework and include frequency-dependence in the self-energy calculations. Our method for the acceleration of static RPA polarizability can be generalized to other frequencies, which will lead to more accurate calculations of open-shell defects.

4. Discussions on the Computational Efficiency

We compare the computational cost of our approaches with that of the direct calculation of the RPA polarizability. For the calculation of the single boron vacancy V_B in monolayer *h*-BN, the direct calculation takes 1,609 core hours and requires 12,679 MB for the memory. As a comparison, the intrinsic screening approximation only takes 57 core hours (excluding the time spent on reciprocal-space folding, which is negligible) and only requires 338 MB for the memory, thanks to the much smaller number of **G** vectors in a unit cell (111 vectors) compared

to that in a supercell (8445 vectors). These two values are 131 core hours and 354 MB for the memory, respectively, for the defect-patched screening approximation. In this example, the calculation used the stampede2 supercomputer (Intel Xeon Phi 7250) at the Texas Advanced Computing Center (TACC). χ_{Defect}^0 includes significantly fewer bands (51 valence bands and 56 conduction bands) compared to 323 valence bands and about 8000 conduction bands in the direct calculation. Therefore, this approach can reduce the computational cost significantly. Moreover, the large memory requirement of direct GW calculations is often the prohibitive factor for routine GW calculations of large supercells. Both the intrinsic screening approximation and the defect-patched screening approximation can reduce the memory requirement by about two orders of magnitude, making the calculations more tractable, even on medium-sized clusters. It is worth mentioning that, in actual calculations, different architecture of the computer cluster can have different performance and wall-time hours. However, the qualitative trend in the overall saving of computational resources should be similar.

5. Conclusion

In this work, we accelerate the GW calculation of defect levels of point defects via approximations to the noninteracting RPA polarizability (χ^0), which is the main bottleneck in large-scale GW calculations. Two levels of approximations are proposed. The first approximation is the intrinsic screening approximation, where χ^0 of the supercell with point defects is replaced by that of a primitive cell via the reciprocal-space folding procedure. The

second approximation is the defect-patched screening approximation, where the defect contribution to the χ^0 is explicitly calculated within a small energy window, which will then be combined with the polarizability of the perfect structure to approximate that of the defect-containing supercell. These approximations substantially reduce the computational cost for RPA polarizability without sacrificing accuracy. We apply this approach to study several typical points defects. We found that for large defect-gap systems, the intrinsic screening approximation is accurate, while for narrow defect-gap systems, it is essential to use the defect-patched screening approximation. We expect that these two approaches are generally applicable to a variety of point defect systems and speed up the search for appropriate defects for desired applications.

FIGURES:

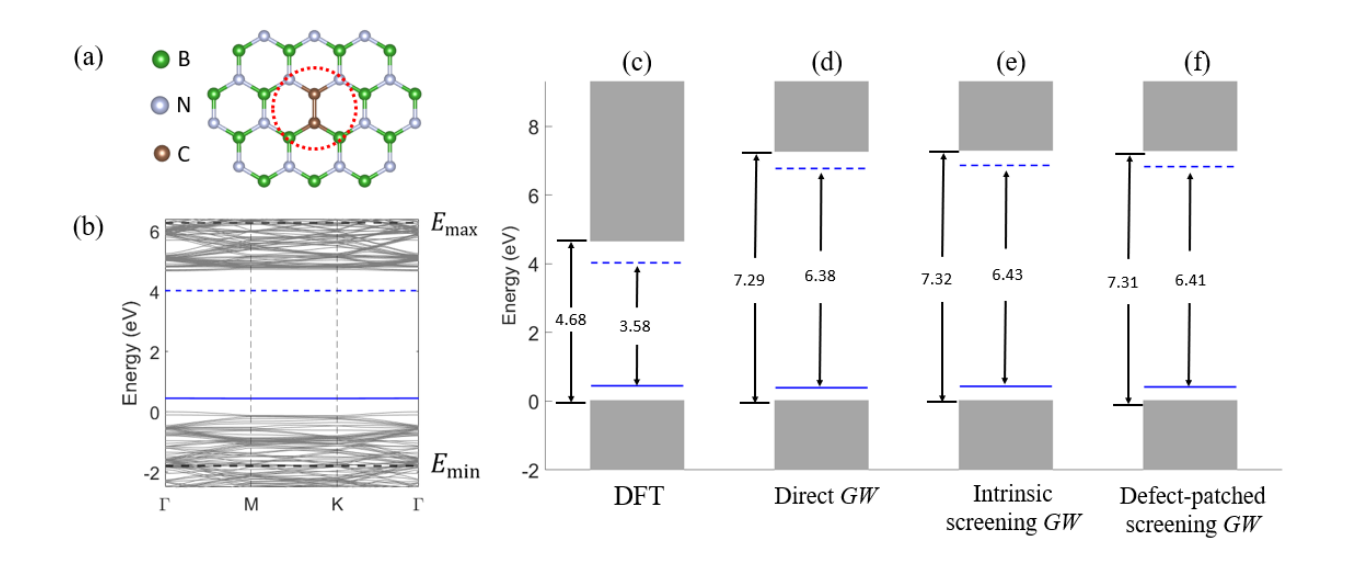


Figure 1. (a) Crystal structure of double carbon substitutional defects (C_BC_N) in monolayer h-BN. The defect site is circled by a red dotted line, where two carbon atoms replace a boron atom and a neighboring nitrogen atom. (b) DFT band structure for the defect system. The grey lines indicate continuum bulk bands and defect states lying inside these continuum bands. The two blue lines indicate in-gap defect states. [E_{\min} , E_{\max}] is the energy window used in the defect-patched screening approximation. Schematic electronic structure of the defect system calculated using (c) DFT, (d) direct GW, (e) intrinsic screening approximation, and (f) defect-patched screening approximation. The solid (dashed) blue line represents the occupied (unoccupied) defect state. The gray boxes represent the continuum bulk bands. The VBM is set to be zero.

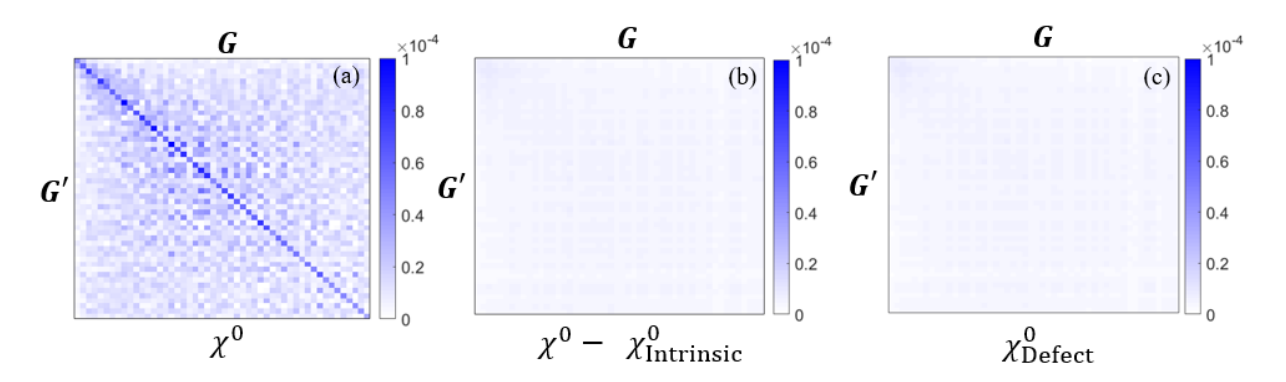


Figure 2. Color maps of the magnitude of matrix elements of the noninteracting RPA polarizability $\chi^0_{GG'}(q=0,\omega=0)$ for a double carbon substitutional defect C_BC_N in monolayer

h-BN. (a) Directly calculated χ^0 of the defect system. (b) $\chi^0 - \chi^0_{\rm Intrinsic}$, which is about two orders of magnitude smaller than the directly calculated χ^0 . (c) Defect contribution to the polarizability, $\chi^0_{\rm Defect}$, which is calculated with Eq. (3). $\chi^0_{\rm Defect}$ is also about two orders of magnitude smaller than the directly calculated χ^0 .

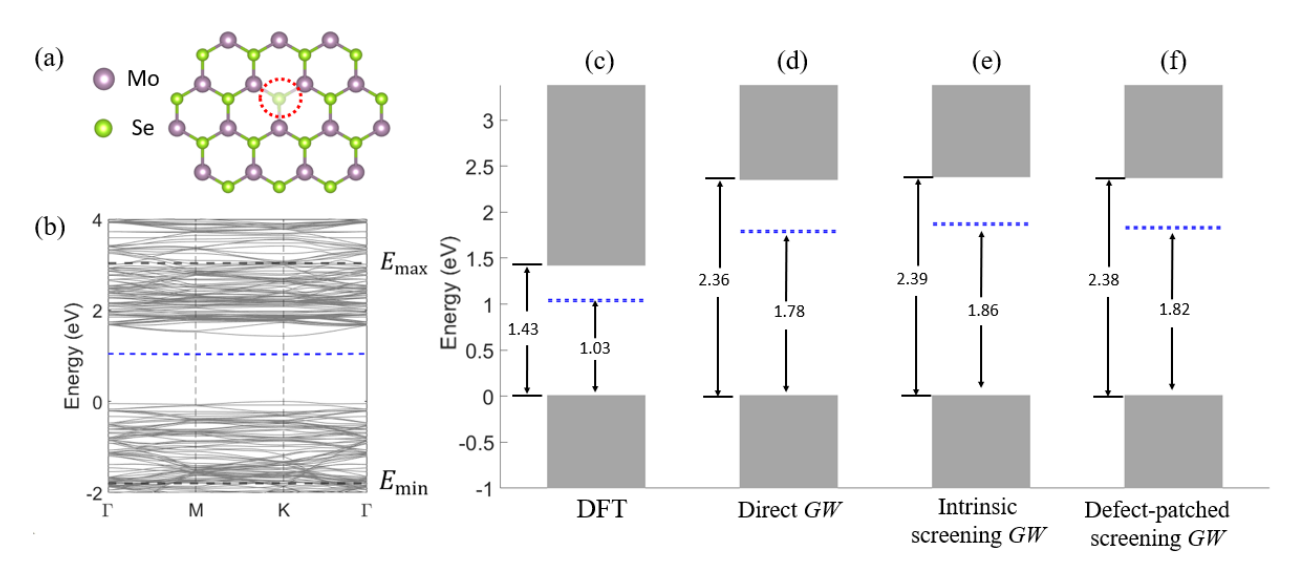


Figure 3. (a) Crystal structure of V_{Se} in monolayer MoSe₂. The defect site is circled by a red dotted line. The half-transparent ball indicates the bottom Se atom, with the top Se atom removed to form a vacancy. (b) DFT band structure for the V_{Se} defect system. The grey lines indicate continuum bulk bands and defect states lying inside the continuum bands. Blue lines indicate in-gap defect states, which are nearly degenerate and unoccupied. [E_{min} , E_{max}] is the energy window used in the defect-patched screening calculation, where E_{max} is set to be 1.6 eV above the CBM, and E_{min} is set to be 1.8 eV below the VBM. Schematic electronic structure

of this defect system calculated using (c) DFT; (d) direct GW; (e) intrinsic screening approximation; and (f) defect-patched screening approximation. The dashed line represents the nearly doubly degenerate unoccupied defect states in the gap. The gray boxes represent the continuum bulk bands. The VBM is set to be zero.

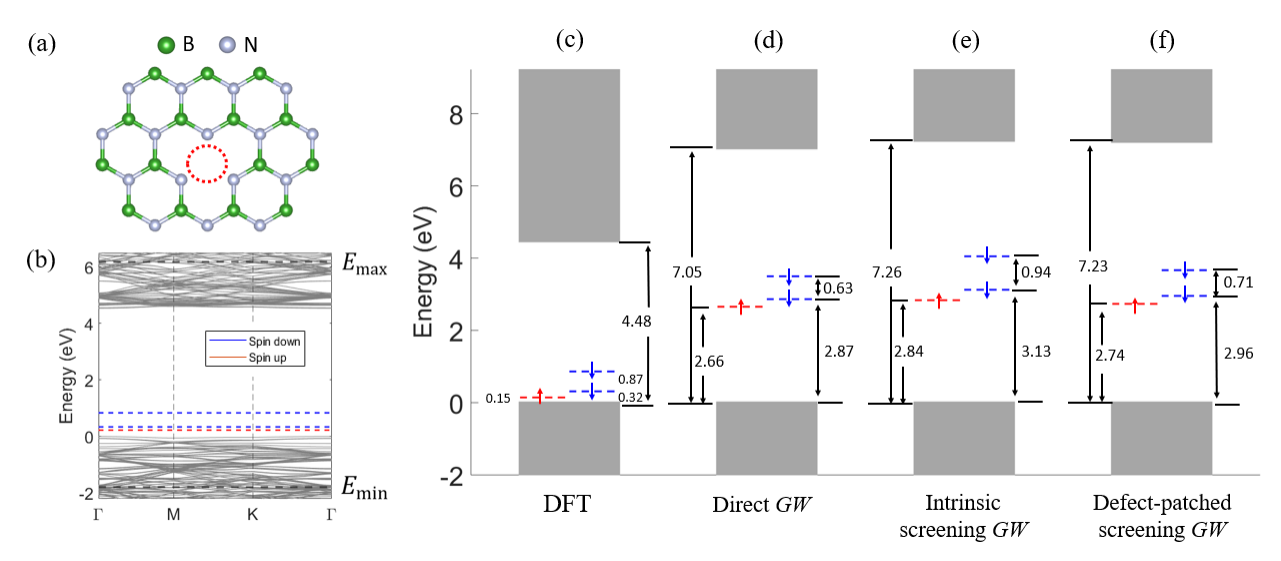


Figure 4. (a) Crystal structure of V_B in monolayer h-BN. The defect site is circled by a red dotted line, where a boron atom is removed. (b) DFT band structure for the V_B defect. The grey lines indicate continuum bulk bands and defect states lying inside the continuum bands. Blue and red lines indicate spin-down and spin-up defect states in the gap, respectively. $[E_{\min}, E_{\max}]$ is the energy window used in the defect-patched screening calculation, where E_{\max} is set to be 1.7 eV above the CBM and E_{\min} is set to be 1.8 eV lower than the VBM. Schematics of the electronic structure calculated from (c) DFT; (d) direct GW; (e) intrinsic screening approximation; and (f) defect-patched screening approximation. The dashed lines represent

unoccupied defect states in the gap, with red (blue) color showing the spin-up (spin-down) bands The gray boxes represent the continuum bulk bands. The VBM is set to be zero.

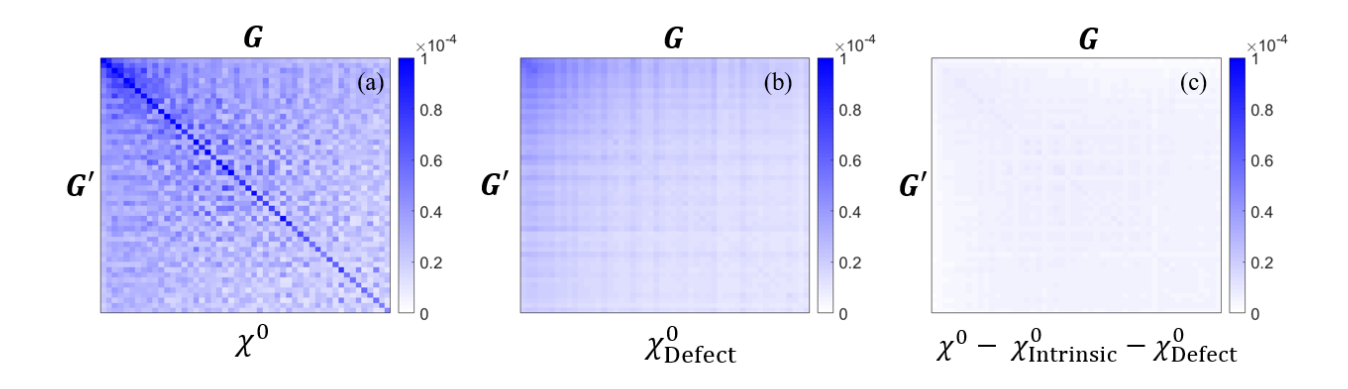


Figure 5. Color maps of the magnitude of matrix elements of the noninteracting RPA polarizability $\chi^0_{GG'}(q=0,\omega=0)$ for a single boron vacancy V_B in monolayer h-BN. (a) Directly calculated χ^0 of the defect system. (b) Defect contribution to the polarizability, χ^0_{Defect} , which is calculated using Eq. (3). (c) Difference between the directly calculated χ^0 for the defect system and the sum of χ^0_{Defect} and $\chi^0_{Intrinsic}$. This is the error in χ^0 from the defect-patched screening approximation.

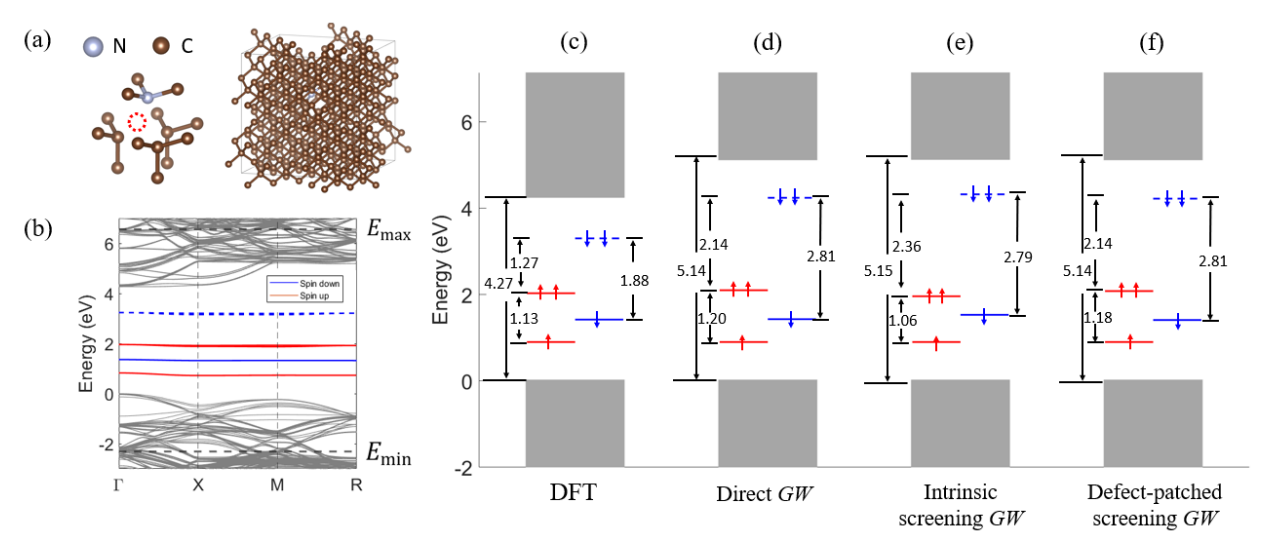


Figure 6. (a) Crystal structure of negatively charged NV center in diamond. The inset shows the detail of the structure of the NV center, where a carbon atom is replaced by a nitrogen atom and the neighboring carbon atom is removed, as shown by the red circle. (b) DFT band structure for the NV center defect structure. The red lines represent spin-up states, and the blue lines represent spin-down states. The grey lines indicate continuum bulk bands and defect states lying inside the continuum bands. $[E_{\min}, E_{\max}]$ is the energy window used in the defect-patched screening calculation, where E_{\max} is set to be 2.3 eV above the CBM and E_{\min} is set to be 2.3 eV below the VBM. Schematics of the defect electronic structure from (c) DFT; (d) direct GW; (e) intrinsic screening approximation; and (f) defect-patched screening approximation. The solid lines represent occupied defect states, and the dashed lines represent unoccupied defect states in the gap. The gray boxes represent the continuum bulk bands. The arrows indicate spin-up (red) or spin-down (blue) states. The VBM is set to be zero.

ASSOCIATED CONTENT

Supporting Information

The relaxed structures of the four point defects studied in the main text, which are used in

the DFT and GW calculations (zip).

AUTHOR INFORMATION

Corresponding Author

*(Z.-F.L.) E-mail: zfliu@wayne.edu

†(L.Y.) E-mail: lyang@physics.wustl.edu

Notes

The authors declare no competing financial interest.

ACKNOWLEDGMENT

D.L. is supported by the National Science Foundation (NSF) grant No. DMR-2124934. L.Y. is

supported by NSF grant No. DMR-2118779. Z.-F.L. is supported by an NSF CAREER award,

DMR-2044552. This work used Anvil at Purdue University through allocation DMR100005

from the Advanced Cyberinfrastructure Coordination Ecosystem: Services & Support

(ACCESS) program,⁷⁹ which is supported by NSF grants #2138259, #2138286, #2138307,

#2137603, and #2138296. Additional computational resources were provided by the Extreme

25

Science and Engineering Discovery Environment (XSEDE), which is supported by NSF Grant No. ACI-1548562 through allocation PHY220043.

REFERENCES

- (1) Dingle, R., Luminescent Transitions Associated with Divalent Copper Impurities and the Green Emission from Semiconducting Zinc Oxide. *Phys. Rev. Lett.* **1969**, *23*, 579-581.
- (2) Meyer, B. K.; Alves, H.; Hofmann, D. M.; Kriegseis, W.; Forster, D.; Bertram, F.; Christen, J.; Hoffmann, A.; Straßburg, M.; Dworzak, M.; Haboeck, U.; Rodina, A. V., Bound Exciton and Donor–Acceptor Pair Recombinations in ZnO. *Phys. Status Solidi B* **2004**, *241*, 231-260.
- (3) Shishonok, E. M.; Steeds, J. W., Near-Threshold Creation of Optical Centres in Electron Irradiated Cubic Boron Nitride. *Diam. Relat. Mater.* **2002**, *11*, 1774-1780.
- (4) Shishonok, E. M., Luminescence Centers in Cubic Boron Nitride. *J. Appl. Spectrosc.* **2007**, *74*, 272-277.
- (5) Tararan, A.; di Sabatino, S.; Gatti, M.; Taniguchi, T.; Watanabe, K.; Reining, L.; Tizei, L. H. G.; Kociak, M.; Zobelli, A., Optical Gap and Optically Active Intragap Defects in Cubic BN. *Phys. Rev. B* **2018**, *98*, 094106.
- (6) Davies, G., Dynamic Jahn-Teller Distortions at Trigonal Optical Centres in Diamond. *J. Phys. C: Solid State Phys.* **1979**, *12*, 2551-2566.
- (7) Davies, G.; Hamer, M. F., Optical Studies of the 1.945 eV Vibronic Band in Diamond. *Proc. R. Soc. Lond. A* **1976**, *348*, 285-298.
- (8) Trusheim, M. E.; Wan, N. H.; Chen, K. C.; Ciccarino, C. J.; Flick, J.; Sundararaman, R.; Malladi, G.; Bersin, E.; Walsh, M.; Lienhard, B.; Bakhru, H.; Narang, P.; Englund, D., Leadrelated Quantum Emitters in Diamond. *Phys. Rev. B* **2019**, *99*, 075430.

- (9) Palyanov, Y. N.; Kupriyanov, I. N.; Borzdov, Y. M.; Surovtsev, N. V., Germanium: A New Catalyst for Diamond Synthesis and A New Optically Active Impurity in Diamond. *Sci. Rep.* **2015**, *5*, 14789.
- (10) Iwasaki, T.; Miyamoto, Y.; Taniguchi, T.; Siyushev, P.; Metsch, M. H.; Jelezko, F.; Hatano, M., Tin-Vacancy Quantum Emitters in Diamond. *Phys. Rev. Lett.* **2017**, *119*, 253601.
- (11) Wrachtrup, J.; Jelezko, F., Processing Quantum Information in Diamond. *J. Phys.: Condens. Matter* **2006**, *18*, S807-S824.
- (12) D'Haenens-Johansson, U. F. S.; Edmonds, A. M.; Green, B. L.; Newton, M. E.; Davies, G.; Martineau, P. M.; Khan, R. U. A.; Twitchen, D. J., Optical Properties of The Neutral Silicon Split-Vacancy Center in Diamond. *Phys. Rev. B* **2011**, *84*, 245208.
- (13) Feng, T.; Schwartz, B. D., Characteristics and origin of the 1.681 eV luminescence center in chemical-vapor-deposited diamond films. *J. Appl. Phys.* **1993**, *73*, 1415-1425.
- (14) Christle, D. J.; Klimov, P. V.; de las Casas, C. F.; Szász, K.; Ivády, V.; Jokubavicius, V.; Ul Hassan, J.; Syväjärvi, M.; Koehl, W. F.; Ohshima, T.; Son, N. T.; Janzén, E.; Gali, Á.; Awschalom, D. D., Isolated Spin Qubits in SiC with a High-Fidelity Infrared Spin-to-Photon Interface. *Phys. Rev. X.* **2017**, *7*, 021046.
- (15) Zargaleh, S. A.; Hameau, S.; Eble, B.; Margaillan, F.; von Bardeleben, H. J.; Cantin, J. L.; Gao, W., Nitrogen Vacancy Center in Cubic Silicon Carbide: A Promising Qubit in the 1.5μm Spectral Range for Photonic Quantum Networks. *Phys. Rev. B* **2018**, *98*, 165203.
- (16) Sörman, E.; Son, N. T.; Chen, W. M.; Kordina, O.; Hallin, C.; Janzén, E., Silicon Vacancy Related Defect in 4H And 6H SiC. *Phys. Rev. B* **2000**, *61*, 2613-2620.
- (17) Falk, A. L.; Klimov, P. V.; Ivády, V.; Szász, K.; Christle, D. J.; Koehl, W. F.; Gali, Á.; Awschalom, D. D., Optical Polarization of Nuclear Spins in Silicon Carbide. *Phys. Rev. Lett.* **2015**, *114*, 247603.
- (18) Koehl, W. F.; Buckley, B. B.; Heremans, F. J.; Calusine, G.; Awschalom, D. D., Room Temperature Coherent Control of Defect Spin Qubits in Silicon Carbide. *Nature* **2011**, *479*, 84-87.
- (19) Gao, W.; da Jornada, F. H.; Del Ben, M.; Deslippe, J.; Louie, S. G.; Chelikowsky, J. R., Quasiparticle Energies and Optical Excitations of 3C-SiC Divacancy from GW and GW Plus Bethe-Salpeter Equation Calculations. *Phys. Rev. Mater.* **2022**, *6*, 036201.
- (20) Awschalom, D. D.; Hanson, R.; Wrachtrup, J.; Zhou, B. B., Quantum Technologies with Optically Interfaced Solid-State Spins. *Nat. Photonics* **2018**, *12*, 516-527.
- (21) Zhang, G.; Cheng, Y.; Chou, J.-P.; Gali, A., Material Platforms for Defect Qubits and Single-Photon Emitters. *Appl. Phys. Rev.* **2020**, *7*, 031308.
- (22) Gali, A., Ab Initio Theory of the Nitrogen-Vacancy Center in Diamond. *Nanophotonics* **2019**, *8*, 1907-1943.

- (23) Doherty, M. W.; Manson, N. B.; Delaney, P.; Jelezko, F.; Wrachtrup, J.; Hollenberg, L. C. L., The Nitrogen-Vacancy Colour Centre in Diamond. *Phys. Rep.* **2013**, *528*, 1-45.
- (24) Ross, J. S.; Klement, P.; Jones, A. M.; Ghimire, N. J.; Yan, J.; Mandrus, D. G.; Taniguchi, T.; Watanabe, K.; Kitamura, K.; Yao, W.; Cobden, D. H.; Xu, X., Electrically Tunable Excitonic Light-Emitting Diodes Based on Monolayer WSe2 p-n Junctions. *Nat. Nanotechnol.* **2014**, *9*, 268-272.
- (25) Palacios-Berraquero, C.; Barbone, M.; Kara, D. M.; Chen, X.; Goykhman, I.; Yoon, D.; Ott, A. K.; Beitner, J.; Watanabe, K.; Taniguchi, T.; Ferrari, A. C.; Atature, M., Atomically Thin Quantum Light-Emitting Diodes. *Nat. Commun.* **2016**, *7*, 12978.
- (26) Chakraborty, C.; Kinnischtzke, L.; Goodfellow, K. M.; Beams, R.; Vamivakas, A. N., Voltage-Controlled Quantum Light from an Atomically Thin Semiconductor. *Nat. Nanotechnol.* **2015**, *10*, 507-511.
- (27) He, Y. M.; Clark, G.; Schaibley, J. R.; He, Y.; Chen, M. C.; Wei, Y. J.; Ding, X.; Zhang, Q.; Yao, W.; Xu, X.; Lu, C. Y.; Pan, J. W., Single Quantum Emitters in Monolayer Semiconductors. *Nat. Nanotechnol.* **2015**, *10*, 497-502.
- (28) Koperski, M.; Nogajewski, K.; Arora, A.; Cherkez, V.; Mallet, P.; Veuillen, J. Y.; Marcus, J.; Kossacki, P.; Potemski, M., Single Photon Emitters in Exfoliated WSe2 Structures. *Nat. Nanotechnol.* **2015**, *10*, 503-506.
- (29) Shaik, A. B. D.; Palla, P., Optical Quantum Technologies with Hexagonal Boron Nitride Single Photon Sources. *Sci. Rep.* **2021**, *11*, 12285.
- (30) Chejanovsky, N.; Rezai, M.; Paolucci, F.; Kim, Y.; Rendler, T.; Rouabeh, W.; Favaro de Oliveira, F.; Herlinger, P.; Denisenko, A.; Yang, S.; Gerhardt, I.; Finkler, A.; Smet, J. H.; Wrachtrup, J., Structural Attributes and Photodynamics of Visible Spectrum Quantum Emitters in Hexagonal Boron Nitride. *Nano Lett.* **2016**, *16*, 7037-7045.
- (31) Tran, T. T.; Bray, K.; Ford, M. J.; Toth, M.; Aharonovich, I., Quantum Emission from Hexagonal Boron Nitride Monolayers. *Nat. Nanotechnol.* **2016**, *11*, 37-41.
- (32) Proscia, N. V.; Shotan, Z.; Jayakumar, H.; Reddy, P.; Cohen, C.; Dollar, M.; Alkauskas, A.; Doherty, M.; Meriles, C. A.; Menon, V. M., Near-Deterministic Activation of Room-Temperature Quantum Emitters in Hexagonal Boron Nitride. *Optica* **2018**, *5*, 1128-1134.
- (33) Exarhos, A. L.; Hopper, D. A.; Grote, R. R.; Alkauskas, A.; Bassett, L. C., Optical Signatures of Quantum Emitters in Suspended Hexagonal Boron Nitride. *ACS Nano* **2017**, *11*, 3328-3336.
- (34) Gottscholl, A.; Kianinia, M.; Soltamov, V.; Orlinskii, S.; Mamin, G.; Bradac, C.; Kasper, C.; Krambrock, K.; Sperlich, A.; Toth, M.; Aharonovich, I.; Dyakonov, V., Initialization and Read-Out of Intrinsic Spin Defects in a van der Waals Crystal at Room Temperature. *Nat. Mater.* **2020**, *19*, 540-545.
- (35) Exarhos, A. L.; Hopper, D. A.; Patel, R. N.; Doherty, M. W.; Bassett, L. C., Magnetic-Field-Dependent Quantum Emission in Hexagonal Boron Nitride at Room Temperature. *Nat. Commun.* **2019**, *10*, 222.

- (36) Chejanovsky, N.; Mukherjee, A.; Geng, J.; Chen, Y. C.; Kim, Y.; Denisenko, A.; Finkler, A.; Taniguchi, T.; Watanabe, K.; Dasari, D. B. R.; Auburger, P.; Gali, A.; Smet, J. H.; Wrachtrup, J., Single-Spin Resonance in a van der Waals Embedded Paramagnetic Defect. *Nat. Mater.* **2021**, *20*, 1079-1084.
- (37) Ivády, V.; Barcza, G.; Thiering, G.; Li, S.; Hamdi, H.; Chou, J.-P.; Legeza, Ö.; Gali, A., Ab Initio Theory of the Negatively Charged Boron Vacancy Qubit in Hexagonal Boron Nitride. *Npj Comput. Mater.* **2020**, *6*, 41.
- (38) Gottscholl, A.; Diez, M.; Soltamov, V.; Kasper, C.; Krausse, D.; Sperlich, A.; Kianinia, M.; Bradac, C.; Aharonovich, I.; Dyakonov, V., Spin Defects in hBN as Promising Temperature, Pressure and Magnetic Field Quantum Sensors. *Nat. Commun.* **2021**, *12*, 4480.
- (39) Reserbat-Plantey, A.; Epstein, I.; Torre, I.; Costa, A. T.; Gonçalves, P. A. D.; Mortensen, N. A.; Polini, M.; Song, J. C. W.; Peres, N. M. R.; Koppens, F. H. L., Quantum Nanophotonics in Two-Dimensional Materials. *ACS Photonics* **2021**, *8*, 85-101.
- (40) Schilfgaarde, V. M.; Kotani, T.; Faleev, S., Quasiparticle Self-consistent GW Theory. *Phys. Rev. Lett.* **2006**, *96*, 226402.
- (41) Goyal, A.; Gorai, P.; Peng, H.; Lany, S.; Stevanović, V., A Computational Framework for Automation of Point Defect Calculations. *Comput. Mater. Sci.* **2017**, *130*, 1-9.
- (42) Hybertsen, M. S.; Louie, S. G., Electron Correlation in Semiconductors and Insulators: Band Gaps and Quasiparticle Energies. *Phys. Rev. B* **1986**, *34*, 5390-5413.
- (43) Hedin, L., New Method for Calculating the One-Particle Green's Function with Application to the Electron-Gas Problem. *Phys. Rev.* **1965**, *139*, A796-A823.
- (44) Barja, S.; Refaely-Abramson, S.; Schuler, B.; Qiu, D. Y.; Pulkin, A.; Wickenburg, S.; Ryu, H.; Ugeda, M. M.; Kastl, C.; Chen, C.; Hwang, C.; Schwartzberg, A.; Aloni, S.; Mo, S. K.; Frank Ogletree, D.; Crommie, M. F.; Yazyev, O. V.; Louie, S. G.; Neaton, J. B.; Weber-Bargioni, A., Identifying Substitutional Oxygen as a Prolific Point Defect in Monolayer Transition Metal Dichalcogenides. *Nat. Commun.* **2019**, *10*, 3382.
- (45) Schuler, B.; Qiu, D. Y.; Refaely-Abramson, S.; Kastl, C.; Chen, C. T.; Barja, S.; Koch, R. J.; Ogletree, D. F.; Aloni, S.; Schwartzberg, A. M.; Neaton, J. B.; Louie, S. G.; Weber-Bargioni, A., Large Spin-Orbit Splitting of Deep In-Gap Defect States of Engineered Sulfur Vacancies in Monolayer WS2. *Phys. Rev. Lett.* **2019**, *123*, 076801.
- (46) Martin-Samos, L.; Roma, G.; Rinke, P.; Limoge, Y., Charged Oxygen Defects in SiO2: Going Beyond Local and Semilocal Approximations to Density Functional Theory. *Phys. Rev. Lett.* **2010**, *104*, 075502.
- (47) Ma, Y.; Rohlfing, M.; Gali, A., Excited States of the Negatively Charged Nitrogen-Vacancy Color Center in Diamond. *Phys. Rev. B* **2010**, *81*, 041204(R).
- (48) Gao, W.; Xia, W.; Gao, X.; Zhang, P., Speeding up GW Calculations to Meet the Challenge of Large Scale Quasiparticle Predictions. *Sci. Rep.* **2016**, *6*, 36849.

- (49) Giustino, F.; Cohen, M. L.; Louie, S. G., GW Method with the Self-consistent Sternheimer Equation. *Phys. Rev. B* **2010**, *81*, 115105.
- (50) Umari, P.; Qian, X.; Marzari, N.; Stenuit, G.; Giacomazzi, L.; Baroni, S., Accelerating GW Calculations with Optimal Polarizability Basis. *Phys. Status Solidi B* **2011**, *248*, 527-536.
- (51) Umari, P.; Stenuit, G.; Baroni, S., GW Quasiparticle Spectra from Occupied States Only. *Phys. Rev. B* **2010**, *81*, 115104.
- (52) Marsili, M.; Mosconi, E.; De Angelis, F.; Umari, P., Large-Scale GW-BSE Calculations with N³ Scaling: Excitonic Effects in Dye-Sensitized Solar Cells. *Phys. Rev. B* **2017**, *95*, 075415.
- (53) Govoni, M.; Galli, G., Large Scale GW Calculations. J. Chem. Theory Comput. 2015, 11, 2680-2696.
- (54) Wilson, H. F.; Gygi, F.; Galli, G., Efficient Iterative Method for Calculations of Dielectric Matrices. *Phys. Rev. B* **2008**, *78*, 113303.
- (55) Nguyen, H.-V.; Pham, T. A.; Rocca, D.; Galli, G., Improving Accuracy and Efficiency of Calculations of Photoemission Spectra within the Many-Body Perturbation Theory. *Phys. Rev. B* **2012**, *85*, 081101(R).
- (56) Pham, T. A.; Nguyen, H.-V.; Rocca, D.; Galli, G., GW Calculations using the Spectral Decomposition of the Dielectric Matrix: Verification, Validation, and Comparison of Methods. *Phys. Rev. B* **2013**, *87*, 155148.
- (57) Neuhauser, D.; Gao, Y.; Arntsen, C.; Karshenas, C.; Rabani, E.; Baer, R., Breaking the Theoretical Scaling Limit for Predicting Quasiparticle Energies: The Stochastic GW Approach. *Phys. Rev. Lett.* **2014**, *113*, 076402.
- (58) Vlček, V.; Rabani, E.; Neuhauser, D.; Baer, R., Stochastic GW Calculations for Molecules. *J. Chem. Theory Comput.* **2017**, *13*, 4997-5003.
- (59) Liu, Z. F.; da Jornada, F. H.; Louie, S. G.; Neaton, J. B., Accelerating GW-Based Energy Level Alignment Calculations for Molecule-Metal Interfaces Using a Substrate Screening Approach. *J. Chem. Theory Comput.* **2019**, *15*, 4218-4227.
- (60) Deslippe, J.; Samsonidze, G.; Strubbe, D. A.; Jain, M.; Cohen, M. L.; Louie, S. G., BerkeleyGW: A Massively Parallel Computer Package for the Calculation of the Quasiparticle and Optical Properties of Materials and Nanostructures. *Comput. Phys. Commun.* **2012**, *183*, 1269-1289.
- (61) Xuan, F.; Chen, Y.; Quek, S. Y., Quasiparticle Levels at Large Interface Systems from Many-Body Perturbation Theory: The XAF-GW Method. *J. Chem. Theory Comput.* **2019**, *15*, 3824-3835.
- (62) Cheng, N. L. Q.; Xuan, F.; Spataru, C. D.; Quek, S. Y., Charge Transfer Screening and Energy Level Alignment at Complex Organic-Inorganic Interfaces: A Tractable Ab Initio GW Approach. *J. Phys. Chem. Lett.* **2021**, *12*, 8841-8846.

- (63) Perdew, J. P.; Burke, K.; Ernzerhof, M., Generalized Gradient Approximation Made Simple. *Phys. Rev. Lett.* **1996**, *77*, 3865-3868.
- (64) Giannozzi, P.; Andreussi, O.; Brumme, T.; Bunau, O.; Buongiorno Nardelli, M.; Calandra, M.; Car, R.; Cavazzoni, C.; Ceresoli, D.; Cococcioni, M.; Colonna, N.; Carnimeo, I.; Dal Corso, A.; de Gironcoli, S.; Delugas, P.; DiStasio, R. A.; Ferretti, A.; Floris, A.; Fratesi, G.; Fugallo, G.; Gebauer, R.; Gerstmann, U.; Giustino, F.; Gorni, T.; Jia, J.; Kawamura, M.; Ko, H. Y.; Kokalj, A.; Küçükbenli, E.; Lazzeri, M.; Marsili, M.; Marzari, N.; Mauri, F.; Nguyen, N. L.; Nguyen, H. V.; Otero-de-la-Roza, A.; Paulatto, L.; Poncé, S.; Rocca, D.; Sabatini, R.; Santra, B.; Schlipf, M.; Seitsonen, A. P.; Smogunov, A.; Timrov, I.; Thonhauser, T.; Umari, P.; Vast, N.; Wu, X.; Baroni, S., Advanced Capabilities for Materials Modelling with Quantum ESPRESSO. *J. Phys.: Condens. Matter* **2017**, *29*, 465901.
- (65) Grimme, S., Semiempirical GGA-Type Density Functional Constructed with a Long-Range Dispersion Correction. *J. Comput. Chem.* **2006**, 27, 1787-1799.
- (66) Deslippe, J.; Samsonidze, G.; Jain, M.; Cohen, M. L.; Louie, S. G., Coulomb-Hole Summations and Energies for GW Calculations with Limited Number of Empty Orbitals: A Modified Static Remainder Approach. *Phys. Rev. B* **2013**, *87*, 165124.
- (67) Ismail-Beigi, S., Truncation of Periodic Image Interactions for Confined Systems. *Phys. Rev.* B **2006**, *73*, 233103.
- (68) Du, X. Z.; Li, J.; Lin, J. Y.; Jiang, H. X., The Origin of Deep-Level Impurity Transitions in Hexagonal Boron Nitride. *Appl. Phys. Lett.* **2015**, *106*, 021110.
- (69) Mackoit-Sinkevičienė, M.; Maciaszek, M.; Van de Walle, C. G.; Alkauskas, A., Carbon Dimer Defect as a Source of the 4.1 Ev Luminescence in Hexagonal Boron Nitride. *Appl. Phys. Lett.* **2019**, *115*, 212101.
- (70) Muechler, L.; Badrtdinov, D. I.; Hampel, A.; Cano, J.; Rösner, M.; Dreyer, C. E., Quantum Embedding Methods for Correlated Excited States of Point Defects: Case Studies and Challenges. *Phys. Rev. B* **2022**, *105*, 235104.
- (71) Refaely-Abramson, S.; Qiu, D. Y.; Louie, S. G.; Neaton, J. B., Defect-Induced Modification of Low-Lying Excitons and Valley Selectivity in Monolayer Transition Metal Dichalcogenides. *Phys. Rev. Lett.* **2018**, *121*, 167402.
- (72) Attaccalite, C.; Bockstedte, M.; Marini, A.; Rubio, A.; Wirtz, L., Coupling of Excitons and Defect States in Boron-Nitride Nanostructures. *Phys. Rev. B* **2011**, *83*, 144115.
- (73) Troullier, N.; Martins, J. L., Efficient Pseudopotentials for Plane-Wave Calculations. *Phys. Rev. B* **1991**, *43*, 1993-2006.
- (74) Strand, J.; Larcher, L.; Shluger, A. L., Properties of Intrinsic Point Defects and Dimers in Hexagonal Boron Nitride. *J. Phys.: Condens. Matter* **2020**, *32*, 055706.
- (75) Lucatto, B.; Assali, L. V. C.; Pela, R. R.; Marques, M.; Teles, L. K., General Procedure for the Calculation of Accurate Defect Excitation Energies from DFT-1/2 Band Structures: The Case of the NV- Center in Diamond. *Phys. Rev. B* **2017**, *96*, 075145.

- (76) Bockstedte, M.; Schütz, F.; Garratt, T.; Ivády, V.; Gali, A., Ab initio Description of Highly Correlated States in Defects for Realizing Quantum Bits. *npj Quantum Mater.* **2018**, *3*, 31.
- (77) Choi, S.; Jain, M.; Louie, S. G., Mechanism for Optical Initialization of Spin in NV- Center in Diamond. *Phys. Rev. B* **2012**, *86*, 041202(R).
- (78) Lischner, J.; Deslippe, J.; Jain, M.; Louie, S. G., First-Principles Calculations of Quasiparticle Excitations of Open-Shell Condensed Matter Systems. *Phys. Rev. Lett.* **2012**, *109*, 036406.
- (79) Boerner, J. T., Deems, S., Furlani, T. R., Knuth, S. L., and Towns, J., **2023**. ACCESS: Advancing Innovation: NSF's Advanced Cyberinfrastructure Coordination Ecosystem: Services & Support. "In Practice and Experience in Advanced Research Computing (PEARC '23)", July 23–27, **2023**, Portland, OR, USA. ACM, New York, NY, USA.